Identifying the Atomic-Level Effects of Metal Composition on the Structure and Catalytic Activity of Peptide-Templated Materials

Nicholas A. Merrill,[†] Erik M. McKee,[†] Kyle C. Merino,[†] Lawrence F. Drummy,[‡] Sungsik Lee,[§] Benjamin Reinhart,[§] Yang Ren,[§] Anatoly I. Frenkel,[⊥] Rajesh R. Naik,[‡] Nicholas M. Bedford,*[,†,‡,∥] and Marc R. Knecht*[,†]

[†]Department of Chemistry, University of Miami, 1301 Memorial Drive, Coral Gables, Florida 33146, United States, [‡]Materials and Manufacturing Directorate, Air Force Research Laboratory, Wright-Patterson Air Force Base, Dayton, Ohio 45433, United States, [§]X-Ray Science Division, Argonne National Laboratory, 9700 S. Cass Avenue, Argonne, Illinois 60439, United States, [⊥]Department of Physics, Yeshiva University, New York, New York 10016, United States, and [∥]Applied Chemicals and Materials Division, National Institute of Standards and Technology, Boulder, Colorado 80305, United States

ABSTRACT

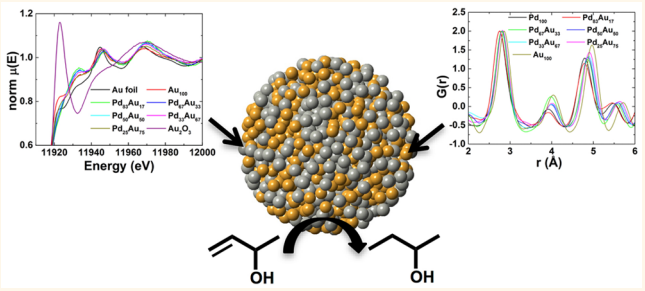

Bioinspired approaches for the formation of metallic nanomaterials have been extensively employed for a diverse range of applications including diagnostics and catalysis. These materials can often be used under sustainable conditions; however, it is challenging to control the material size, morphology, and composition simultaneously. Here we have employed the R5 peptide, which forms a 3D scaffold to direct the size and linear shape of bimetallic PdAu nanomaterials for catalysis. The materials were prepared at varying Pd:Au ratios to probe optimal compositions to achieve maximal catalytic efficiency. These materials were extensively characterized at the atomic level using transmission electron microscopy, extended X-ray absorption fine structure spectroscopy, and atomic pair distribution function analysis derived from high-energy X-ray diffraction patterns to provide highly resolved structural information. The results confirmed PdAu alloy formation, but also demonstrated that significant surface structural disorder was present. The catalytic activity of the materials was studied for olefin hydrogenation, which demonstrated enhanced reactivity from the bimetallic structures. These results present a pathway to the bioinspired production of multimetallic materials with enhanced properties, which can be assessed *via* a suite of characterization methods to fully ascertain structure/function relationships.

KEYWORDS: bimetallic nanostructures · peptide templates · bioinspired · X-ray analysis · catalysis

Metallic nanomaterials have great potential to advance catalytic applications, where the next grand challenge arises from the ability to control their composition and surface structure at the atomic level. Research has shown that the catalytic activity of nanomaterials is directly dependent upon the particle size, composition, shape, and arrangement of atoms at the nanoparticle surface.[1−4] To optimize their catalytic activity, enhanced structural control at the atomic level is necessary, thus requiring new synthetic methods. One avenue toward addressing these structural effects is through the fabrication of bimetallic catalysts that possess enhanced reactivity as compared to their monometallic counterparts from two different effects: changes in the material electronic structure and/or the geometric arrangement of the two metal components to generate active sites. In the former, alteration of

* Address correspondence to nicholas.bedford@nist.gov, knecht@miami.edu.

Received for review July 27, 2015 and accepted October 23, 2015.

Published online October 23, 2015
10.1021/acsnano.5b04665

the electronic properties of the catalytically active metal is achieved that leads to enhanced reactivity. For example, the inclusion of small amounts of Au to catalytic Pd materials leads to increased turnover, where the more electronegative Au pulls electron density from the Pd to increase reactivity.[5,6] The same is true when a small amount of Pd or Pt is added to Au nanocatalysts.[7,8] For the geometric arrangement effect, the two metals are combined in such a way to form new active sites.[6,9] While bimetallic nanoparticles are clearly of increasing scientific interest for the development of sustainable catalysts, new synthesis techniques are required for their direct fabrication. Furthermore, fundamental structural studies at the atomic level are greatly needed to fully correlate composition and metallic structure to the catalytic properties. Without such information, the generation of new catalytic materials with enhanced reactivity will be limited.

While numerous routes are known for the fabrication of nanoscale materials, biomimetic approaches for nanoparticle synthesis have become increasingly popular due to the structural diversity that can be achieved through the noncovalent interaction of biomolecules at inorganic interfaces.[10,11] In this regard, a variety of biological capping agents including proteins,[12,13] peptides,[14,15] and DNA[16] have been explored for the fabrication of inorganic materials. Peptides are of particular interest due to the potential for materials property manipulation through rational sequence design. This modularity of peptides is attractive, as sequence design strategies can be implemented to optimize catalytic properties through the manipulation of the biotic/abiotic interface.[10,17−19] In this regard, the peptide sequence has recently been demonstrated to possess the ability to create active sites at the atomic scale on nanoparticle surfaces.[10]

Beyond the binding of biomolecules directly to nanoparticle interfaces, the diverse functionality found in nature can invoke the formation of larger, self-assembled scaffolds to template nanomaterials.[20−25] Such effects have been observed for cage proteins such as ferritin[25−28] or clathrin;[20,29−31] however, self-assembling peptides are also able to facilitate biotemplation. One such peptide is R5 (SSKKSGSYSGSKGSKRRIL), a fragment of the silifin-1 protein responsible for SiO_2 precipitation in the diatom *Cylindrothica fusiformis*.[32,33] Due to the −RRIL motif, the peptide is able to aggregate in solution in an inverse micelle-like structure.[14,23,24,34] To this end, the hydrophobic residues arrange at the core of the structure, thus exposing the polar amino acids to solution. This biotemplate can facilitate the formation of monometallic nanomaterials as shown previously for Pd, Pt, and Au.[23,24,34] The size and morphology of the materials can be controlled by varying the inorganic composition and metal:R5 ratio, leading to the formation of spherical nanoparticles, nanoribbons, or nanoparticle networks (NPNs).[23,24,34] For Pd-based structures, at low Pd:R5 ratios, spherical nanoparticles are formed inside the bioscaffold where the particles are highly dispersed; however, as the Pd:R5 ratio increases, a greater particle density is achieved. This positions the materials closer together, eventually leading to linear aggregation to form nanoribbons at a Pd:R5 ratio of 90 and fused NPNs at a ratio of 120.[14,24] Interestingly, the morphology of Au nanomaterials fabricated with the R5 scaffold was quite different, where only NPNs were noted regardless of the metal:R5 ratio, indicating that the inorganic composition played an important role in controlling the material morphology.[24,34]

In this contribution, the R5 bioscaffold was used to template highly catalytic bimetallic PdAu nanostructures. While holding the metal loading within the template constant, the Pd:Au ratio was varied from 100% Pd to 100% Au, leading to significant morphological changes in the final zerovalent structures; Pd nanoparticles were observed that gradually changed into NPNs as the amount of Au in the material increased. All of the materials were extensively characterized using energy-dispersive X-ray spectroscopy (EDS) mapping, extended X-ray absorption fine-structure spectroscopy (EXAFS), and atomic pair distribution function (PDF) analysis of high-energy X-ray diffraction (HE-XRD) patterns. Modeling of the PDF and EXAFS data provided atomic-scale material configurations where the degree of bimetallic miscibility was fully resolved. The results indicated that the R5-templated PdAu nanocatalysts were largely alloyed with minor phase separation noted at certain Pd:Au ratios. The catalytic activity of these alloyed structures was assessed using olefin hydrogenation as a model reaction, where the reactivity demonstrated enhanced turnover frequency (TOF) values for the nanostructures generated at a Pd:Au ratio of 2:1. From the combination of high-resolution characterization techniques, this study provides key atomic structural evidence for the understanding of bimetallic nanocatalysis. Furthermore, the effects of material composition on biotemplation is demonstrated, indicating that the interactions between the metal and peptide framework play a critical role in controlling material morphology and reactivity.

RESULTS AND DISCUSSION

The general approach for the fabrication of R5-templated bimetallic materials is shown in Scheme 1. Due to the-RRIL motif, the peptide self-assembles into a large bioscaffold in water (~960 nm),[34] where the polar residues are available to template nanomaterials, as shown previously for monometallic Pd, Au, and Pt.[23,24,34,35] To create bimetallic nanocatalysts of two noble metals (*i.e.*, PdAu) within the R5 template, Pd^{2+} and Au^{3+} ions were commixed and allowed to

complex with the bioscaffold. After complexation, the metal ions were reduced with excess $NaBH_4$. In this approach, both the Pd^{2+} and Au^{3+} species in the template are simultaneously reduced, which typically results in the generation of alloyed bimetallic materials.[36−42] Synthesis of core−shell-type structures (*i.e.*, monometallic Au materials surrounded by a Pd shell) was attempted *via* a sequential fabrication strategy; however, the materials precipitated after the reduction of the second material, limiting the analysis to those structures generated *via* co-reduction. For the present study, all samples were synthesized with 60 total metal ions per peptide where the Pd:Au ratios varied from 100% Pd to 100% Au. To distinguish between the different samples, the following nomenclature will be used: Pd_xAu_y where *x* and *y* represent the ratio of Pd to Au atoms out of 100 total atoms employed during material fabrication, which effectively represents the percent composition. For monometallic materials, they are specifically referred to as Pd_{100} or Au_{100}. Inductively coupled plasma mass spectrometry (ICP-MS) was performed on all samples before and after dialysis, which demonstrated that their expected stoichiometries were maintained (Supporting Information, Table S1).

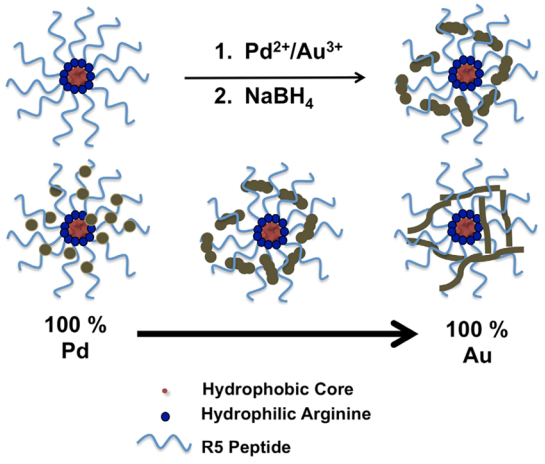

Scheme 1. Mechanism for the formation of PdAu bimetallic materials employing the R5 template.

Figure 1 presents the UV−vis analysis of the R5-templated bimetallic materials before and after reduction with $NaBH_4$. Prior to reduction for the Pd_{100} sample (Figure 1a), a ligand-to-metal charge transfer (LMCT) band was observed at 235 nm corresponding to the interactions between Pd^{2+} and the R5 template, consistent with previous studies.[14] As Au^{3+} is introduced to the biotemplate, such as in the $Pd_{83}Au_{17}$ sample, the Pd^{2+} LMCT band decreases concomitantly with the formation of peaks at 220 and 291 nm for the Au^{3+} within the bioscaffold.[34] As the amount of Au^{3+} increases, the 235 nm peak continues to decrease with an increase in the 220 and 291 nm peaks, as anticipated based upon the material composition. After reduction (Figure 1b), the LMCT bands disappear, suggestive of metal ion reduction, where the spectra observed are nearly featureless for all of the samples. An increase in absorbance toward lower wavelengths consistent with nanomaterial production, however, is noted for each material.[43] Interestingly, for the Au_{100} sample, a broad plasmon band is noted at wavelengths > 500 nm, as observed previously,[34] but no similar observation is noted for any of the other samples, even those with a high Au composition.

To confirm the production of metallic nanomaterials employing the R5 scaffold, TEM imaging was used. Figure 2 presents the images of the different materials, where additional TEM images at higher magnifications and material size histograms are shown in the Supporting Information, Figures S1 and S2. From this study, the size and morphology of the nanocatalysts can be ascertained, where clear structural shifts were observed as a function of the metallic composition. Small nearly spherical nanoparticles of 3.0 ± 0.7 nm were observed for the Pd_{100} materials (Figure 2a), consistent with previously reported values.[23,24] Upon introduction of Au in the $Pd_{83}Au_{17}$ materials, no significant change in particle shape or size (3.0 ± 0.6 nm) was observed (Figure 2b). Further increases in the relative Au loading in the sample demonstrated an interesting shift in morphology for the metallic materials. In this regard, small nanoribbons were formed where the average ribbon width increased as the amount of Au

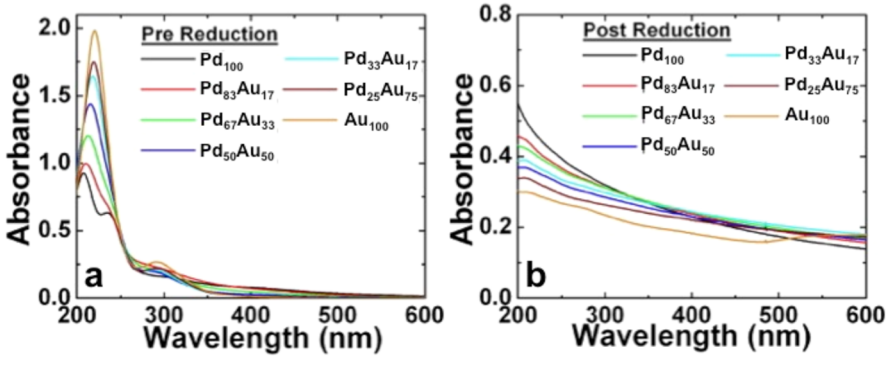

Figure 1. UV−vis analysis of the R5-templated PdAu structures (a) before and (b) after reduction.

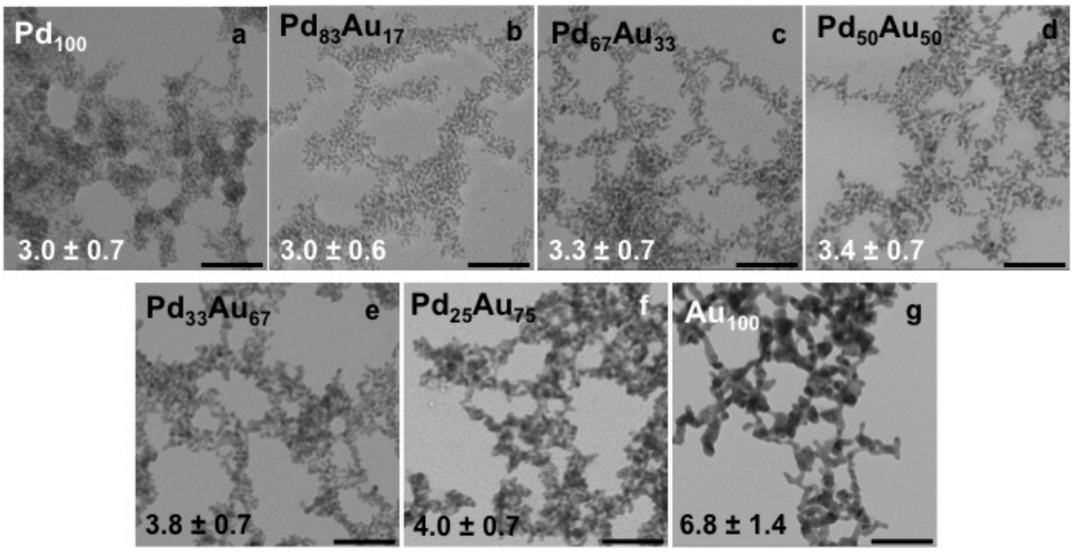

Figure 2. TEM images of the (a) Pd_{100}, (b) $Pd_{83}Au_{17}$, (c) $Pd_{67}Au_{33}$, (d) $Pd_{50}Au_{50}$, (e) $Pd_{33}Au_{67}$, (f) $Pd_{25}Au_{75}$, and (g) Au_{100} samples. Scale bar = 50 nm.

in the sample increased (3.3 ± 0.7, 3.4 ± 0.7, and 3.8 ± 0.7 nm for the $Pd_{67}Au_{33}$, $Pd_{50}Au_{50}$, and $Pd_{33}Au_{67}$ samples, respectively, Figure 2c–e). For the samples with the two highest amounts of Au, $Pd_{25}Au_{75}$, and Au_{100}, only NPNs were formed with an average width of 4.0 ± 0.7 and 6.8 ± 1.4 nm, respectively (Figure 2f and g). This trend indicates that as the amount of Au in the sample increases, the tendency to form linearized nanostructures also increases. In general, the materials go from small mostly spherical structures for the monometallic Pd_{100} sample to nanoribbons at intermediate $Pd_{50}Au_{50}$ materials to full NPNs in the Au_{100} samples. Such structural results are consistent with previous studies of monometallic Pd and Au systems using the R5 framework, indicating that the metal composition is important in controlling the morphology of the inorganic structure.[14,34]

While UV–vis and TEM confirmed the formation of nanomaterials *via* the co-reduction approach, the metallic composition and atomic arrangement of the Pd and Au atoms within the structures must be assessed using different methods. Such information is critically important, especially at the atomic level with nanoscale spatial resolution, in order to accurately correlate the structure/function/reactivity relationship of nanomaterials. As such, a suite of complementary methods was explored to fully examine the atomic-scale metallic structures of the PdAu materials. Initially EDS mapping was conducted, as shown in Figure 3, to visualize the degree of atomic mixing within the materials. Figure 3a specifically presents a STEM image of the $Pd_{67}Au_{33}$ materials. High-resolution imaging of the structure, shown in the Supporting Information, Figure S3, was used to measure the lattice spacing, which was found to be 2.3 Å, corresponding to the fcc (111) mixed crystal lattice of a PdAu alloy.[44] Figure 3b and c present the

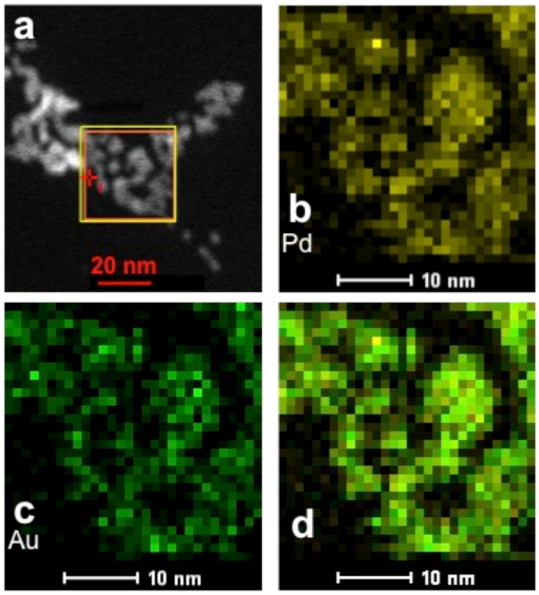

Figure 3. EDS mapping analysis of the $Pd_{67}Au_{33}$ sample. (a) STEM image of the structure that was mapped. (b and c) Pd and Au elemental mapping, respectively. (d) Overlay of the Pd and Au maps displaying the mixing of the two metals in the structure.

elemental mapping of Pd and Au, respectively, while Figure 3d shows an overlay of the two elemental maps. The EDS mapping indicates an overlap in the Pd and Au signal, suggesting that the Pd and Au are distributed throughout the structure, reminiscent of an alloyed material. As both Pd^{2+} and Au^{3+} were introduced to the R5 template prior to reduction, such a result was expected, as Pd and Au are known to alloy.[42,45] While such a technique suggests alloy formation, it is unable to fully resolve the atomic level interactions between the Pd and Au atoms of the structure; thus higher resolution spectroscopic and diffraction studies are

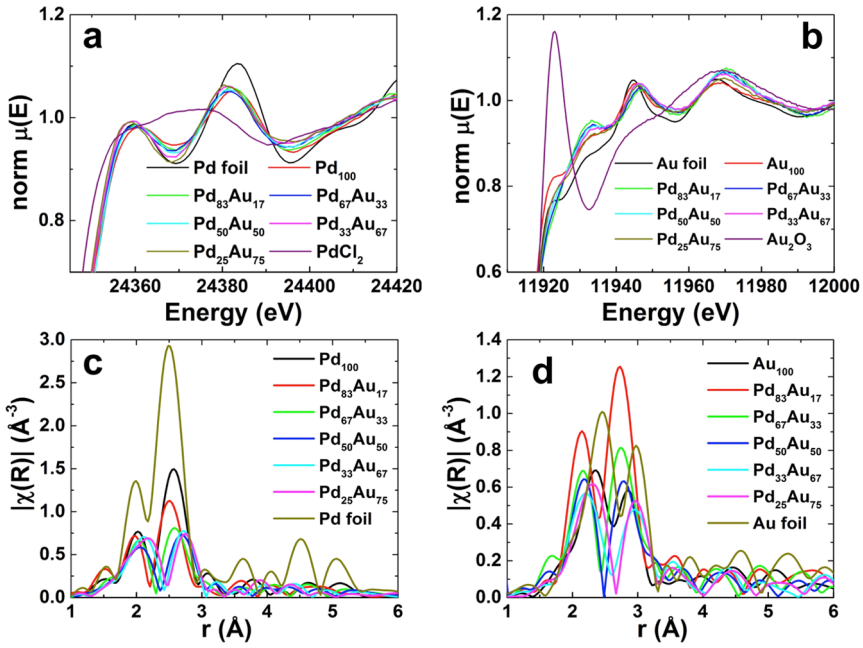

Figure 4. XAFS analysis of the R5-templated PdAu bimetallic materials: XANES data at the (a) Pd K-edge and (b) Au L_3-edge; EXAFS *r*-space data at the (c) Pd K-edge and (d) Au L_3-edge.

required to probe the metal arrangement of the materials at the atomic level.

To understand the role of the R5 template in controlling the resultant morphology and atomic-scale structure of the PdAu materials, rigorous X-ray-based studies were performed. To this end, X-ray absorption fine-structure (XAFS) spectroscopy was used to provide local chemical and structural information on an element-specific basis. X-ray energies were scanned from ~200 eV below to ~900 eV above each element's absorption edge, as shown in the Supporting Information, Figure S4. The X-ray absorption near-edge structure (XANES) spectra around the Pd K-edge (24.35 keV) indicate that the Pd is largely metallic, as compared to bulk Pd, with a slight shift to lower energies with increasing Au content (Figure 4a). Comparison of the PdAu materials to $PdCl_2$ as a reference for Pd^{2+} further indicates that nearly all the Pd^{2+} is reduced to Pd^0. The XANES data taken around the Au L_3-edge (11.92 keV) show a similar trend, wherein the catalysts are largely metallic with shifts in absorption features to higher energy with increasing Pd content (Figure 4b). A slight Au-nonmetal feature at 11,920 eV is present in the Au_{100} sample (as compared to Au_2O_3 as a Au^{3+} reference), which may be due to the presence of unreduced Au^{3+}.

After background subtraction and edge-step normalization, the EXAFS data were converted to *k*-space and k^2-weighted (Supporting Information, Figure S5), then Fourier transformed to *r*-space (Figure 4c and d). For the Pd foil standard, a main peak position is 2.45 Å, which corresponds to the Pd−Pd first nearest neighboring bond (Figure 4c). Note that due to photoelectron phase shift, uncorrected for in the Fourier transform, this position is lower than the Pd−Pd bulk distance of 2.74 Å. For the $Pd_{83}Au_{17}$ nanomaterials, this peak generally maintained its position, while the samples produced with increasing amounts of Au tended to shift this peak toward larger distances. Qualitatively, this indicates that the Pd environment is becoming more Au-rich, because the interatomic distance in pure bulk Au (2.87 Å) is larger than in pure bulk Pd.

Probing these materials around the Au L_3-edge provides complementary information (Figure 4d). The split peak (the splitting originates from the well-known Townsend−Ramsauer resonance) from the Au foil standard represents the nearest neighbor Au−Au bond length. As the amount of Pd is increased in these materials, this peak moves to shorter distances. Taken together, this peak shifting observation qualitatively suggests that the Pd and Au are miscible in these materials, thus forming an alloyed structure. It is worth noting that the distances of the monometallic systems (Pd_{100} and Au_{100}) exhibit slight *r*-space shifts away from their respective reference foils. The Pd−Pd bond length becomes slightly longer in Pd_{100}, while the Au−Au bond length in Au_{100} becomes more constricted. Nearest neighbor distances in nanomaterials are known to frequently differ from the bulk, as shown previously.[46−48]

The EXAFS data were next modeled with the Artemis program[49] (Supporting Information Figures S6 and S7) using only metal−metal contributions to provide element-specific coordination numbers (CNs), which are reported in Table 1 and Figure 5. For Pd_{100}, a Pd−Pd CN of 7.48 ± 0.54 was obtained, which is lower than the expected theoretical value of 9.63 for a spherical

TABLE 1. Structure Metrics from EXAFS Modeling and RMC Simulations of PDFs

catalyst	Pd−Pd CN	Pd−Au CN	Au−Pd CN	Au−Au CN	Pd:Au stoichiometric ratio	Pd:Au surface ratio from RMC
Pd_{100}	7.48 ± 0.54	0	0	0		
$Pd_{83}Au_{17}$	6.58 ± 0.53	2.10 ± 0.48	7.25 ± 1.03	2.20 ± 1.28	5.0	5.0
$Pd_{67}Au_{33}$	4.09 ± 0.48	5.00 ± 0.64	5.32 ± 0.91	6.84 ± 3.43	2.0	2.70
$Pd_{50}Au_{50}$	4.47 ± 0.98	4.98 ± 0.96	3.60 ± 0.78	6.58 ± 2.15	1.0	1.28
$Pd_{33}Au_{67}$	2.42 ± 0.49	7.12 ± 0.67	2.29 ± 0.29	7.77 ± 0.87	0.50	0.68
$Pd_{25}Au_{75}$	2.55 ± 1.77	8.68 ± 1.36	1.68 ± 0.39	7.74 ± 0.79	0.33	0.30
Au_{100}	0	0	0	9.31 ± 0.78		

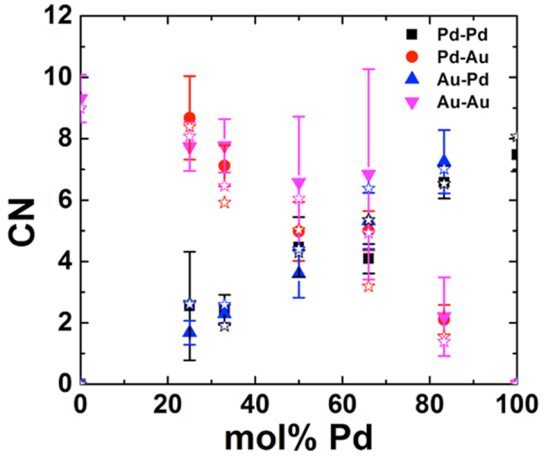

Figure 5. CN values obtained from EXAFS modeling for Pd−Pd (black squares), Pd−Au (red circles), Au−Pd (blue triangles), and Au−Au (pink triangles). Hollow stars represent CNs resulting from RMC modeling of the PDF data (same color code as EXAFS-generated CNs).

crystalline nanoparticle of this size.[50] The fact that coordination numbers appear to be smaller than those predicted from average particle sizes can originate from either or both of the following effects. The first effect is the broad size distribution that includes small metal species and/or unreduced ions that are not detectable by STEM. In that case the average particle size inferred from the coordination number analysis will be smaller than that obtained by STEM.[51] The second effect is due to the asymmetric bond length disorder that can mimic the reduction in coordination numbers as obtained by conventional EXAFS analysis of nanoparticles.[52] In this case, due to the monodisperse particle size distribution (Figure 2), the apparent reduction of the coordination number from what is expected from the STEM-obtained average size is likely due to a certain degree of structural disorder, which we recently discovered in another set of peptide-capped Pd nanoparticles,[10] and is also shown for the R5-templated materials with reverse Monte Carlo (RMC) modeling of PDF data (see below). For random nanoalloys, an increase in the Au concentration results in bimetallic CNs that change linearly with atomic percentage,[53] as shown in Figure 5. In this regard, as the amount of Au in the sample increases, the Pd−Pd CN values linearly decrease and the Au−Au CNs increase due to the greater amount of Au in the materials. For the Au_{100} sample, a Au−Au CN of 9.31 ± 0.78 was obtained. Approximating the NPNs to spheres of comparable diameters, this CN is within error of expected values for materials of this size. When considering the Pd−Au and Au−Pd CN values, the trends are consistent with the values anticipated for random alloys as a function of metal concentration. In this regard, the Pd−Au CN values (a central Pd atom with a Au nearest neighbor) increased with greater amounts of Au in the sample, while the Au−Pd CNs (a central Au atom with a Pd nearest neighbor) decreased. These trends support the formation of a PdAu alloy, where deviations from linearity are anticipated for nonalloyed structures (*i.e.*, phase segregated or core−shell materials),[36] as well as the artifacts of the EXAFS analysis that are described above. Interestingly, all calculated CNs for $Pd_{67}Au_{33}$ tend to fall slightly off this linear trend (Figure 5), suggesting either a possibility of a higher degree of phase separation in these materials or the effects due to the analysis artifacts (*vide supra*); however, the associated error bars from this data set indicate that complete miscibility may still be a possibility

While EXAFS analysis can provide atomic-scale details of the first coordination sphere for bimetallic systems, detailed structural information at length scales approaching the dimensions of the nanomaterial are not obtainable. Such information is important to elucidate total nanoscale structural knowledge in order to fully assess structure/function relationships. To obtain atomic-scale structural information over larger length scales, PDF analysis of HE-XRD patterns was performed (Figure 6). PDF analysis can provide sub-angstrom structural information over much larger length scales and is well suited for materials lacking long-range periodic order, such as nanoparticles.[54] HE-XRD analysis of the bimetallic materials was studied from lyophilized samples (Supporting Information, Figure S8), converted into total structure functions (Supporting Information, Figure S9), and Fourier transformed into atomic PDFs. The PDFs, $G(r) = 4\pi r[\rho(r) - \rho_0]$, exhibit peaks when the local atomic density is higher than the average atomic density and oscillate to zero once the average and local atomic densities are equal, signifying the distance at which any long-range order is present.

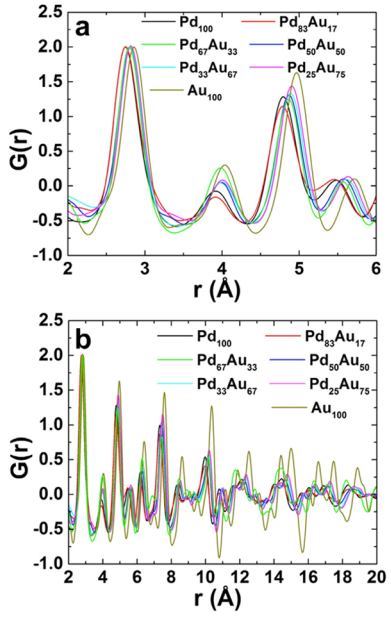

Figure 6. PDFs for R5-templated PdAu bimetallic structures up to (a) 6 Å and (b) 20 Å to illustrate structural differences at various length scales.

Figure 6 shows the PDFs for all of the R5-templated bimetallic nanocatalysts up to 6 and 20 Å to show structural differences at various length scales. Figure S10 of the Supporting Information presents the PDFs up to 35 Å for a full comparison. For Pd_{100} and $Pd_{83}Au_{17}$, the peak representing the first coordination sphere is measured at 2.74 Å (Figure 6), signifying that the minority Au atoms sit within a Pd fcc-type structure in the $Pd_{83}Au_{17}$ nanoparticles. The first peak in the PDF for $Pd_{67}Au_{33}$ and $Pd_{50}Au_{50}$ shifts to 2.80 Å, while $Pd_{33}Au_{67}$ and $Pd_{25}Au_{75}$ shift even further to 2.82 Å. This indicates that as the amount of Au increases in the catalyst, the structure becomes more Au-like in nature and is fully consistent with the EXAFS data. Au_{100} has a first peak 2.86 Å, which is the distance for the first coordination sphere for a Au fcc-structured material. The shifts in peak positions become larger from Pd-heavy to Au-heavy nanocatalysts at longer pair distances due to the spacing difference between a Pd fcc-like structure and Au fcc-like structure. Additionally, changes to the peak shape exhibited at various length scales in the catalysts are present, suggesting structural variations may be influenced by the R5 template.

While PDF analysis can provide long-range structural details of the bimetallic nanocatalysts, there is no direct route for obtaining CNs that described the local atomic environment from the PDFs. This presents a challenge in obtaining accurate nanostructural models from atomic PDFs, as qualitative insights may bias the structure modeling. In this instance, however, the CNs obtained from the EXAFS analysis can be used in the PDF modeling in a direct, systematic fashion. To accomplish this, RMC simulations were employed. RMC is an established technique for modeling nanostructures at the atomic scale,[10,55−58] wherein atoms in a model system are moved at random and a new theoretical PDF is calculated. If the new theoretical PDF begins to converge to the experimental PDF, then the move is accepted; otherwise it is rejected within a certain probability to prevent the simulation from becoming stuck in a local minimum. This algorithm is repeated until the PDF calculated from RMC converges to the experimental PDF. Here, we use the CNs obtained from EXAFS modeling as a constraint to drive RMC simulations that reasonably fit the PDF data (Supporting Information, Figure S11) while satisfying the CNs from EXAFS experiments (Table 1). By combining structural data at various length scale, more realistic structural models can be obtained that could otherwise not be with either method alone.

RMC models of each bimetallic nanocatalyst, approximated to a sphere for simplicity, are shown in Figure 7 (additional models are shown in the Supporting Information, Figure S12, and monometallic materials are also shown in the Supporting Information, Figure S13), while the reported CNs from RMC are shown as stars in Figure 5. All material configurations exhibit a fair amount of surface structural disorder, particularly for the smaller, more Pd-rich samples. Quartered models illustrate a more ordered core of metal atoms than those at the surface. Visually, these models verify a more or less miscible Pd−Au alloy at all compositions. Note that CNs calculated from the RMC-generated models are very close to those calculated from EXAFS modeling (Figure 5). In particular, $Pd_{67}Au_{33}$ exhibits a mostly alloyed structure, with CNs calculated from RMC modeling falling within the linear CN trend of metallic composition; these RMC-generated CNs fall within the error of the EXAFS-calculated CNs. Calculation of the stoichiometric ratio at the surface of the materials was determined where there is a slight bias of Pd segregation to the surface (Table 1), with $Pd_{67}Au_{33}$ demonstrating the furthest deviation from the material synthesis stoichiometry (2 Pd:1 Au) with a Pd:Au surface atom ratio of 2.70. In the context of previous studies, theoretical predictions suggest Pd is likely to phase separate on the basis of comparative cohesive energy and atomic radii,[59] which can explain the varying degrees of minor surface segregation. The local chemical environment (stabilizing moiety, solvent, substrate molecules, *etc*.) can also affect the surface structure by more strongly interacting with a particular element in the bimetallic structure, inducing phase separation.[60] To our knowledge, the biotemplated PdAu nanomaterials are unique, and thus a direct comparison to previous literature of other biotemplated bimetallic materials is not possible; however, nonbiological organic stabilizers and templates have also demonstrated slight Pd surface segregation.[40,42] Taken together, the combination of EXAFS

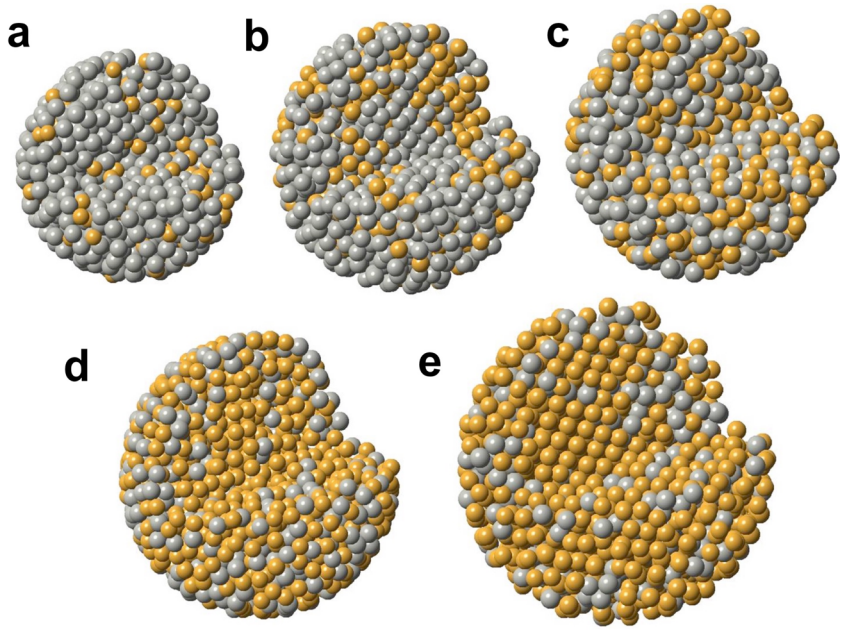

Figure 7. R5-templated PdAu bimetallic materials generated by RMC modeling of the PDF data for (a) $Pd_{83}Au_{17}$, (b) $Pd_{67}Au_{33}$, (c) $Pd_{50}Au_{50}$, (d) $Pd_{33}Au_{67}$, and (e) $Pd_{25}Au_{75}$

and PDF data with RMC simulations provides nanomaterial configurations that can help assess structure/function relationships for the development of new materials with improved catalytic properties.

To assess the catalytic activity of the R5-templated PdAu nanomaterials, olefin hydrogenation was employed as a model catalytic reaction. Previously, we reported on R5-templated monometallic Pd nanostructures that exhibited modestly high TOFs for the hydrogenation of allyl alcohol (~2900 mol product (mol Pd × h)$^{-1}$).[24] The inclusion of Au to a Pd catalyst can significantly affect the electronics of the materials whereby the more electronegative Au can pull electron density away from the Pd, thus making it more catalytically reactive.[5,37] As shown in Figure 8, the inclusion of Au into the Pd nanocatalysts results in increased TOFs at certain Pd:Au ratios. Figure 8a shows the TOF values for the hydrogenation of allyl alcohol using the R5-templated bimetallic materials. A TOF of 2936 ± 72 mol product (mol Pd × h)$^{-1}$ was determined for the monometallic Pd_{100} nanoparticles, consistent with previous results.[24] Upon introduction of a small amount of Au into the material ($Pd_{83}Au_{17}$), no significant difference in the TOF was observed; however, for the $Pd_{67}Au_{33}$ sample, a near 2-fold enhancement in reactivity was observed with a TOF of 5535 ± 142 mol product (mol Pd × h)$^{-1}$. As the Au loading within the sample increased, a substantial decrease in reactivity was noted with no catalytic turnover observed for the $Pd_{33}Au_{67}$, $Pd_{25}Au_{75}$, and Au_{100} materials. Such a lack of reactivity from the materials with high Au loadings was not surprising, as Au is not typically reactive for olefin hydrogenation under these conditions.

To confirm that the reactivity increase was related to the alloyed bimetallic materials, the same reaction was studied using physical mixtures of the R5-templated monometallic Au and Pd materials. For this, the Pd_{100} and Au_{100} samples were prepared separately and then mixed in the hydrogenation reaction at the same metal loading and Pd:Au atomic ratios of the bimetallic materials. From this physical mixture system, no reactivity enhancements were noted where the TOF values linearly decreased as the amount of Au increased in the reaction. This strongly supports the fact that the Pd and Au components are alloyed together in the materials to allow for the electronic changes leading to the enhanced reactivity.

Our results using allyl alcohol as the substrate demonstrate enhanced reactivity is observed when ~33% of the inorganic material is Au. These observations correspond well with trends presented by Scott *et al.*, who synthesized PdAu bimetallic alloys in dendrimer templates.[37] In their work, an increase in the TOF for the conversion of allyl alcohol to 1-propanol was observed for samples with less than 50% Au in the nanoparticles.[37] With this, the largest increase in TOF was observed for the materials with ~63% Pd and 37% Au, similar to the present results.[37] In a separate study, Toshima *et al.* prepared polyvinylpyrrolidone (PVP)-capped PdAu nanoparticles and found an increase in the turnover frequency (TOF) for Pd-rich nanoparticles for the hydrogenation of 1,3-cyclooctadiene.[61] They found that particles with a Pd:Au ratio of 80:20 showed the largest increase in TOF of approximately 25% over comparable monometallic Pd materials with a steady decrease in reactivity as the Au mol % increased.[61] This effect is quite reminiscent of the observations of the

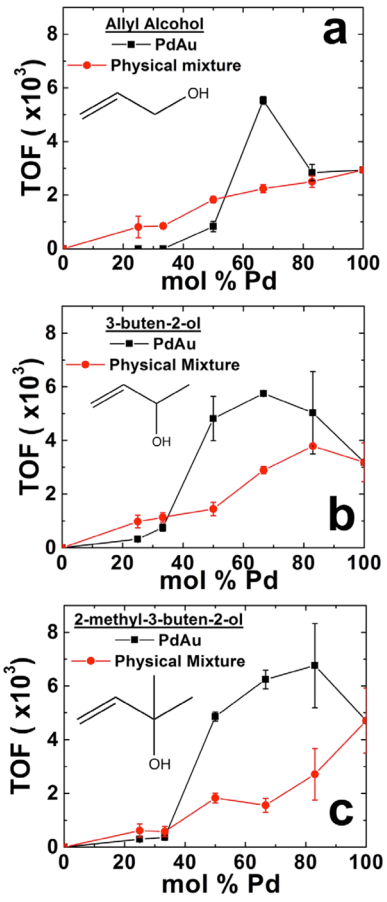

Figure 8. Catalytic analysis of the R5-templated PdAu materials for the olefin hydrogenation of (a) allyl alcohol, (b) 3-buten-2-ol, and (c) 2-methyl-3-buten-2-ol. The black plots show the catalytic analysis of the bimetallic structures, while the red plots present the reactivity of a physical mixture of R5-templated Pd and Au monometallic structures at the same metal concentration used for the bimetallic materials.

peptide-templated materials. In other work by Dash *et al.*, PVP-stabilized PdAu nanomaterials were synthesized in 1-butyl-3-methylimidazolium hexafluorophosphate ionic liquid and used for the hydrogenation of olefinic alcohols.[62] In this work, they observed the largest increase (~50%) in catalytic activity for particles containing ~25% Au for each substrate tested.[62] This study demonstrates that the electronic enhancement effects can be applied to a wide array of reaction conditions. In general, our results for the peptide-templated PdAu materials are quite similar to previous studies, supporting an enhanced reactivity from the bimetallic structures.

We have previously shown that the size and structure of the olefinic alcohol substrate significantly contribute to the hydrogenation reactivity.[35] Such effects arise from isomerization events that are driven at the catalytic surface, thus abating the intended hydrogenation reaction. To observe if similar effects played a role with the PdAu bimetallic structures, the hydrogenation of 3-buten-2-ol and 2-methyl-3-buten-2-ol, a secondary and tertiary alcohol, respectively, was studied. In general, a similar reactivity trend was observed for the secondary and tertiary alcohol substrates as compared to allyl alcohol, where the TOF values increased with greater fractions of Pd in the bimetallic structure. Furthermore, for both of these substrates, enhanced reactivity was noted when <50% of the metallic composition of the PdAu structures was Au. More specifically for 3-buten-2-ol (Figure 8b), a TOF of 3182 ± 727 mol product (mol Pd × h)$^{-1}$ was observed for the Pd_{100} materials, consistent with previous studies.[35] As the Au fraction increased, greater TOF values of 5031 ± 1536 and 5750 ± 28 mol product (mol Pd × h)$^{-1}$ were noted for the $Pd_{83}Au_{17}$ and $Pd_{67}Au_{33}$ samples, respectively. As the Au composition of the bimetallic materials increased to 50% and higher, the TOF rapidly decreased to 323 ± 27 mol product (mol Pd × h)$^{-1}$ for the $Pd_{25}Au_{75}$ sample, with no reactivity for the monometallic Au_{100} materials. When studying the tertiary alcohol, 2-methyl-3-buten-2-ol (Figure 8c), the Pd_{100} sample gave rise to significant catalytic reactivity with a TOF of 4707 ± 1206 mol product (mol Pd × h)$^{-1}$. Maximal reactivity for this substrate was noted from the $Pd_{83}Au_{17}$ materials (TOF = 6737 ± 1571 mol product (mol Pd × h)$^{-1}$), where the reactivity steadily decreased for this substrate as the concentration of Au in the materials increased. As with the other substrates, no reaction was observed for the tertiary alcohol using the monometallic Au_{100} NPNs. For both the 3-buten-2-ol and 2-methyl-3-buten-2-ol substrates, when physical mixture controls were studied, the reactivity rapidly decreased as a function of the amount of monometallic Au in the reaction, consistent with the allyl alcohol studies, reconfirming the effects of the alloyed structure on the material reactivity.

As the substrate was changed from a primary to tertiary alcohol, noticeable differences in the catalytic reactivity were observed. In this regard, higher TOF values were noted for the more substituted substrates. This effect was due to the differences in the isomerization of the reagents; however, this process did not abate the enhanced reactivity effects of the bimetallic structures. It has been previously shown that the degree of substrate isomerization during the reaction plays an important role in the resulting TOF. In this regard, Pacardo *et al.* demonstrated that for the selected substrates, the primary alcohol (allyl alcohol) isomerizes to the anticipated aldehyde significantly more than the secondary alcohol (3-buten-2-ol) under these reaction conditions. Interestingly, the tertiary alcohol substrate (2-methyl-3-buten-2-ol) is not observed to isomerize.[35] On this basis, a portion of the catalytic surface area is consumed for isomerization and unavailable for the actual hydrogenation process, thus inhibiting reaction progression. As a result, the TOF value is directly related to substrate isomerization whereby substrates with greater degrees of

isomerization display lower TOF values. Such effects were again observed herein with the PdAu structures.

CONCLUSION

In summary, PdAu bimetallic alloy nanocatalysts were generated using biotemplating approaches. In this regard, a peptide scaffold was used to coload both Pd^{2+} and Au^{3+} ions, which, upon reduction, resulted in nanomaterial generation. The morphology of the final structures was strictly dependent upon the metallic composition where nanoparticles are generated at high Pd loadings that became NPNs at high Au loadings. The materials were extensively characterized at the atomic level using both electron microscopy and X-ray-based methods, which supported the formation of alloyed bimetallic PdAu materials with minor Pd surface enhancement. Interestingly, significant metal atom structural disorder was noted at the material surface, which is infrequently considered when studying nanomaterials for catalysis. Catalytic application of the PdAu biotemplated structures for olefin hydrogenation demonstrated enhanced reactivity at Au loadings of ~30%. This enhancement likely lies in electronic changes to the Pd component driven *via* electronegativity differences between Pd and Au, thus making the Pd more reactive for hydrogenation. Taken together, these studies demonstrate the effects of biotemplatation on bimetallic nanomaterial production, which indicated that such materials could be readily produced with interesting properties. The significant structural characterization provided unique information on the materials at the atomic level, fully confirming the structural morphology and the effects of the biotemplate over the material structure, displaying significant atomic surface structural disorder. This suggests that such effects could be adapted to other multimetallic systems for applications beyond catalysis, including optics, biosensing, electronics, *etc.*, which could be readily controlled by the material composition.

MATERIALS AND METHODS

Chemicals. K_2PdCl_4, $HAuCl_4$, allyl alcohol, 3-buten-2-ol, 2-methyl-3-buten-2-ol, and antifoam SE-15 were purchased from Sigma-Aldrich. $NaBH_4$ was purchased from Acros Organics. Wang resins and FMOC-protected amino acids were purchased from Advanced Chemtech. The solvents used in peptide synthesis, including methanol, *N*,*N*-dimethylformamide (DMF), and acetonitrile, were purchased from VWR. All materials were used as received. MilliQ water (18 MΩ cm) was used for all experiments.

Peptide Synthesis. The R5 peptide was synthesized and cleaved on a TETRAS synthesizer (Creosalus) using standard FMOC protocols and purified using reversed-phase HPLC.[63] Peptide molecular weights were confirmed using MALDI-TOF mass spectrometry.

Synthesis of R5-Templated Bimetallic PdAu Nanomaterials. The synthesis approach for the PdAu bimetallic materials was adapted from previously published methods.[14,37] All materials were synthesized at a 60:1 total metal:R5 ratio, where the Pd:Au ratio varied from 1:0 (Pd_{100}), 5:1 ($Pd_{83}Au_{17}$), 2:1 ($Pd_{67}Au_{33}$), 1:1 ($Pd_{50}Au_{50}$), 1:2 ($Pd_{33}Au_{67}$), 1:3 ($Pd_{25}Au_{75}$), and 0:1 (Au_{100}). Briefly, 4.93 μL of a 10 mg/mL R5 stock solution was added to 3.00 mL of water. Next, 14.70, 12.25, 9.80, 7.35, 4.90, 3.68, or 0.00 μL of a 0.10 M stock solution of K_2PdCl_4 in water was added to the peptide solution, followed by 0.00, 2.45, 4.90, 7.35, 9.80, 11.03, or 14.70 μL of a 0.10 M stock of aqueous $HAuCl_4$ for each respective ratio. After stirring for 15.0 min at room temperature, 75.0 μL of freshly prepared 0.10 M $NaBH_4$ was added to reduce the metal ions. The PdAu materials were allowed to reduce at room temperature for 1.0 h and then dialyzed overnight to remove any excess reagents.

Catalytic Hydrogenation Experiments. Catalytic hydrogenation of olefinic alcohols was conducted as previously described with minor modifications.[24,64] Briefly, 1.28 mL of the bimetallic materials was added to 23.72 mL of water and 20.0 μL of antifoam SE-15 in a 250 mL three-necked round-bottom flask. H_2 gas was then bubbled through a glass gas dispersion tube at a 50 kPa gauge pressure for 30 min to fully saturate the metal surface with H atoms, followed by the addition of 25.0 mL of a 50.0 mM solution of allyl alcohol, 3-buten-2-ol, or 2-methyl-3-buten-2-ol to start the reaction. In this setup, a 0.05 mol % metal catalyst loading was employed for all reactions. An aliquot was immediately extracted to represent a 0 min time point, followed by aliquot removal at 1, 5, 10, 15, 20, 30, 40, 50, and 60 min. To assess the TOF of the reaction, the aliquots were analyzed by a gas chromatograph (GC, Agilent 7820A), which was equipped with a DB-ALC1 column and a flame ionization detector.

Characterization. UV−vis analysis was performed on an Agilent 8453 system using a 2.0 mm quartz cuvette. Before use, all cuvettes were cleaned with aqua regia. ICP-MS experiments were performed on all bimetallic nanomaterial samples before and after dialysis. Nanomaterial solutions (50 μL) were digested in 100 μL of freshly prepared concentrated aqua regia for 5 h. The samples were then diluted with 1.0 mL of H_2O for ICP-MS experimentation. Experiments were performed at the University of Colorado at Boulder's Laboratory for Environmental and Geological Studies using a Perkin-Elmer SCIEX instrument. TEM images were obtained using a Phillips CM200 system operating at 200 kV. Samples were prepared by drop casting 5 μL of each nanomaterial solution onto a Cu TEM grid (200 mesh, Ted Pella). An FEI Titan was used for high-resolution TEM (HRTEM) imaging and elemental mapping using EDS, wherein samples were prepared on amorphous silicon grids (SimPore Inc.). EXAFS was performed at the 12-BM beamline, Advanced Photon Source, Argonne National Laboratory. Lyophilized powders were spread across Scotch tape for analysis, and both the Pd K-edge and Au L_3-edge were examined 200 eV before to 900 eV after each element adsorption edge. X-ray fluorescence data were collected using a 13-channel Ge detector. The raw data were processed using the Athena program and modeled with FEFF6 theory using the Artemis program from the IFEFFIT XAFS analysis software.[49] Data of standard foils of Pd and Au were first analyzed to obtain S_0^2 values of 0.844 and 0.827 for Pd and Au, respectively. HE-XRD experiments were performed at the 11-ID-C beamline of the Advanced Photon Source, Argonne National Laboratory. Lyophilized powders were loaded into 2 mm quartz capillaries to obtain diffraction patterns at very high Q (~45 $Å^{-1}$) using 115 keV irradiation. The HE-XRD patterns were converted into atomic pair distribution functions using the program RAD.[65] Briefly, HE-XRD patterns were background subtracted and converted into structure functions *via*

$$S(Q) = 1 + \frac{I^{coh}(Q) - \sum c_i |f_i(Q)|^2}{|\sum c_i f_i(Q)|^2} \quad (1)$$

wherein $I^{coh}(Q)$ is the coherent part of the HE-XRD pattern and c_i and $f_i(Q)$ are the atomic concentration and X-ray scattering factors, respectively, for the atomic species *i*. The atomic pair

distribution functions, $G(r)$, were obtained from the Fourier transform of $Q[S(Q) - 1]$ *via*

$$G(r) = \left(\frac{2}{\pi}\right) \int_{Q=0}^{Q_{max}} Q[S(Q) - 1]\sin(Qr)\, dQ \qquad (2)$$

Here $G(r)$ is defined as $G(r) = 4\pi r[\rho(r) - \rho_0]$, wherein $\rho(r)$ is the atomic density at distance r and ρ_0 is the average atomic density in the sample. To obtain nanostructure configurations, atomic PDF data were modeled with RMC simulations using RMC++,[66] wherein the CNs obtained from EXAFS were used to guide the RMC simulations in obtaining structurally accurate degrees of alloying. Truncates of ideal crystals were used as starting structure consisting of a random distribution of Pd and Au atoms. For materials with a Pd composition > 50%, a Pd lattice was used as starting structure, while a Au lattice was used for all other samples.

Conflict of Interest: The authors declare no competing financial interest.

Supporting Information Available: The Supporting Information is available free of charge on the ACS Publications website at DOI: 10.1021/acsnano.5b04665.

ICP-MS data, additional TEM images, particle-sizing histograms, HR-TEM analysis of $Pd_{67}Au_{33}$ materials, XAS spectra, *k*-space analysis, EXAFS modeling, HE-XRD patterns, total structure functions, PDF graphs at 35 Å, RMC model fits, and bimetallic and monometallic RMC models (PDF)

Acknowledgment. This work was supported in part by the National Science Foundation (MRK: DMR-1145175) and the Air Force Office of Scientific Research (RRN). N.M.B. acknowledges fellowship support from National Research Council Associateship award during the initial phases of this work. A.I.F. acknowledges funding by the Division of Chemical Sciences, Geosciences, and Biosciences within the U.S. Department of Energy Office of Basic Energy Sciences, Grant No. DE-FG02-03ER15476. Use of the Advanced Photon Source, an Office of Science User Facility operated for the U.S. Department of Energy (DOE) Office of Science by Argonne National Laboratory, was supported by the U.S. DOE under Contract No. DE-AC02-06CH11357.

REFERENCES AND NOTES

1. Zhou, X.; Xu, W.; Liu, G.; Panda, D.; Chen, P. Size-Dependent Catalytic Activity and Dynamics of Gold Nanoparticles at the Single-Molecule Level. *J. Am. Chem. Soc.* **2010**, *132*, 138–146.
2. Roduner, E. Size Matters: Why Nanomaterials are Different. *Chem. Soc. Rev.* **2006**, *35*, 583–592.
3. Pérez, Y.; Ruiz-González, M. L.; González-Calbet, J. M.; Concepción, P.; Boronat, M.; Corma, A. Shape-Dependent Catalytic Activity of Palladium Nanoparticles Embedded in SiO_2 and TiO_2. *Catal. Today* **2012**, *180*, 59–67.
4. Chen, W.; Kim, J.; Sun, S.; Chen, S. Composition Effects of FePt Alloy Nanoparticles on the Electro-Oxidation of Formic Acid. *Langmuir* **2007**, *23*, 11303–11310.
5. Toshima, N.; Yonezawa, T. Bimetallic Nanoparticles-Novel Materials for Chemical and Physical Applications. *New J. Chem.* **1998**, *22*, 1179–1201.
6. Tao, F. Synthesis, Catalysis, Surface Chemistry and Structure of Bimetallic Nanocatalysts. *Chem. Soc. Rev.* **2012**, *41*, 7977–7979.
7. Qian, H.; Jiang, D.-e.; Li, G.; Gayathri, C.; Das, A.; Gil, R. R.; Jin, R. Monoplatinum Doping of Gold Nanoclusters and Catalytic Application. *J. Am. Chem. Soc.* **2012**, *134*, 16159–16162.
8. Qian, H.; Barry, E.; Zhu, Y.; Rongchao, J. Doping 25-Atom and 38-Atom Gold Nanoclusters with Palladium. *Acta Phys-Chim. Sin.* **2011**, *27*, 513–519.
9. Toshima, N.; Wang, Y. Polymer-Protected Cu/Pd Bimetallic Clusters. *Adv. Mater.* **1994**, *6*, 245–247.
10. Bedford, N. M.; Ramezani-Dakhel, H.; Slocik, J. M.; Briggs, B. D.; Ren, Y.; Frenkel, A. I.; Petkov, V.; Heinz, H.; Naik, R. R.; Knecht, M. R. Elucidation of Peptide-Directed Palladium Surface Structure for Biologically Tunable Nanocatalysts. *ACS Nano* **2015**, *9*, 5082–5092.
11. Tang, Z.; Palafox-Hernandez, J. P.; Law, W.-C.; Hughes, Z. E.; Swihart, M. T.; Prasad, P. N.; Knecht, M. R.; Walsh, T. R. Biomolecular Recognition Principles for Bionanocombinatorics: An Integrated Approach To Elucidate Enthalpic and Entropic Factors. *ACS Nano* **2013**, *7*, 9632–9646.
12. Qin, L.-X.; Li, Y.; Li, D.-W.; Jing, C.; Chen, B.-Q.; Ma, W.; Heyman, A.; Shoseyov, O.; Willner, I.; Tian, H.; Long, Y.-T. Electrodeposition of Single-Metal Nanoparticles on Stable Protein 1 Membranes: Application of Plasmonic Sensing by Single Nanoparticles. *Angew. Chem., Int. Ed.* **2012**, *51*, 140–144.
13. Klem, M. T.; Mosolf, J.; Young, M.; Douglas, T. Photochemical Mineralization of Europium, Titanium, and Iron Oxyhydroxide Nanoparticles in the Ferritin Protein Cage. *Inorg. Chem.* **2008**, *47*, 2237–2239.
14. Jakhmola, A.; Bhandari, R.; Pacardo, D. B.; Knecht, M. R. Peptide Template Effects for the Synthesis and Catalytic Application of Pd Nanoparticle Networks. *J. Mater. Chem.* **2010**, *20*, 1522–1531.
15. Graf, P.; Mantion, A.; Haase, A.; Thünemann, A. F.; Mašić, A.; Meier, W.; Luch, A.; Taubert, A. Silicification of Peptide-Coated Silver Nanoparticles—A Biomimetic Soft Chemistry Approach toward Chiral Hybrid Core−Shell Materials. *ACS Nano* **2011**, *5*, 820–833.
16. Barrett, L.; Dougan, J. A.; Faulds, K.; Graham, D. Stable Dye-Labelled Oligonucleotide-Nanoparticle Conjugates for Nucleic Acid Detection. *Nanoscale* **2011**, *3*, 3221–3227.
17. Coppage, R.; Slocik, J. M.; Ramezani-Dakhel, H.; Bedford, N. M.; Heinz, H.; Naik, R. R.; Knecht, M. R. Exploiting Localized Surface Binding Effects to Enhance the Catalytic Reactivity of Peptide-Capped Nanoparticles. *J. Am. Chem. Soc.* **2013**, *135*, 11048–11054.
18. Coppage, R.; Slocik, J. M.; Sethi, M.; Pacardo, D. B.; Naik, R. R.; Knecht, M. R. Elucidation of Peptide Effects that Control the Activity of Nanoparticles. *Angew. Chem., Int. Ed.* **2010**, *49*, 3767–3770.
19. Li, Y.; Tang, Z.; Prasad, P. N.; Knecht, M. R.; Swihart, M. T. Peptide-Mediated Synthesis of Gold Nanoparticles: Effects of Peptide Sequence and Nature of Binding on Physicochemical Properties. *Nanoscale* **2014**, *6*, 3165–3172.
20. Schoen, A. P.; Huggins, K. N. L.; Heilshorn, S. C. Engineered Clathrin Nanoreactors Provide Tunable Control Over Gold Nanoparticle Synthesis and Clustering. *J. Mater. Chem. B* **2013**, *1*, 6662–6669.
21. Kramer, R. M.; Li, C.; Carter, D. C.; Stone, M. O.; Naik, R. R. Engineered Protein Cages for Nanomaterial Synthesis. *J. Am. Chem. Soc.* **2004**, *126*, 13282–13286.
22. Douglas, T.; Strable, E.; Willits, D.; Aitouchen, A.; Libera, M.; Young, M. Protein Engineering of a Viral Cage for Constrained Nanomaterials Synthesis. *Adv. Mater.* **2002**, *14*, 415–418.
23. Bhandari, R.; Knecht, M. R. Effects of the Material Structure on the Catalytic Activity of Peptide-Templated Pd Nanomaterials. *ACS Catal.* **2011**, *1*, 89–98.
24. Bhandari, R.; Pacardo, D. B.; Bedford, N. M.; Naik, R. R.; Knecht, M. R. Structural Control and Catalytic Reactivity of Peptide-Templated Pd and Pt Nanomaterials for Olefin Hydrogenation. *J. Phys. Chem. C* **2013**, *117*, 18053–18062.
25. Douglas, T.; Dickson, D. P. E.; Betteridge, S.; Charnock, J.; Garner, C. D.; Mann, S. Synthesis and Structure of an Iron(III) Sulfide-Ferritin Bioinorganic Nanocomposite. *Science* **1995**, *269*, 54–57.
26. Douglas, T.; Stark, V. T. Nanophase Cobalt Oxyhydroxide Mineral Synthesized within the Protein Cage of Ferritin. *Inorg. Chem.* **2000**, *39*, 1828–1830.
27. Galvez, N.; Sanchez, P.; Dominguez-Vera, J. M. Preparation of Cu and CuFe Prussian Blue Derivative Nanoparticles Using the Apoferritin Cavity as Nanoreactor. *Dalton Trans.* **2005**, 2492–2494.
28. Galvez, N.; Sanchez, P.; Dominguez-Vera, J. M.; Soriano-Portillo, A.; Clemente-Leon, M.; Coronado, E. Apoferritin-Encapsulated Ni and Co Superparamagnetic Nanoparticles. *J. Mater. Chem.* **2006**, *16*, 2757–2761.

29. Sadasivan, S.; Patil, A. J.; Bromley, K. M.; Hastie, P. G. R.; Banting, G.; Mann, S. Novel Protein-Inorganic Nanoparticles Prepared by Inorganic Replication of Self-Assembled Clathrin Cages and Triskelia. *Soft Matter* **2008**, *4*, 2054–2058.
30. Huggins, K. N. L.; Schoen, A. P.; Arunagirinathan, M. A.; Heilshorn, S. C. Multi-Site Functionalization of Protein Scaffolds for Bimetallic Nanoparticle Templating. *Adv. Funct. Mater.* **2014**, *24*, 7737–7744.
31. Schoen, A. P.; Schoen, D. T.; Huggins, K. N. L.; Arunagirinathan, M. A.; Heilshorn, S. C. Template Engineering Through Epitope Recognition: A Modular, Biomimetic Strategy for Inorganic Nanomaterial Synthesis. *J. Am. Chem. Soc.* **2011**, *133*, 18202–18207.
32. Poulsen, N.; Sumper, M.; Kröger, N. Biosilica Formation in Diatoms: Characterization of Native Silaffin-2 and its Role in Silica Morphogenesis. *Proc. Natl. Acad. Sci. U. S. A.* **2003**, *100*, 12075–12080.
33. Kröger, N.; Lorenz, S.; Brunner, E.; Sumper, M. Self-Assembly of Highly Phosphorylated Silaffins and Their Function in Biosilica Morphogenesis. *Science* **2002**, *298*, 584–586.
34. Bhandari, R.; Knecht, M. R. Synthesis, Characterization, and Catalytic Application of Networked Au Nanostructures Fabricated Using Peptide Templates. *Catal. Sci. Technol.* **2012**, *2*, 1360–1366.
35. Pacardo, D. B.; Ardman, E.; Knecht, M. R. Effects of Substrate Molecular Structure on the Catalytic Activity of Peptide-Templated Pd Nanomaterials. *J. Phys. Chem. C* **2014**, *118*, 2518–2527.
36. Knecht, M. R.; Weir, M. G.; Frenkel, A. I.; Crooks, R. M. Structural Rearrangement of Bimetallic Alloy PdAu Nanoparticles within Dendrimer Templates to Yield Core/Shell Configurations. *Chem. Mater.* **2008**, *20*, 1019–1028.
37. Scott, R. W. J.; Wilson, O. M.; Oh, S.-K.; Kenik, E. A.; Crooks, R. M. Bimetallic Palladium–Gold Dendrimer-Encapsulated Catalysts. *J. Am. Chem. Soc.* **2004**, *126*, 15583–15591.
38. Hamill, C.; Burch, R.; Goguet, A.; Rooney, D.; Driss, H.; Petrov, L.; Daous, M. Evaluation and Mechanistic Investigation of a AuPd Alloy Catalyst for the Hydrocarbon Selective Catalytic Reduction (HC-SCR) of NO_x. *Appl. Catal., B* **2014**, *147*, 864–870.
39. Scott, R. W. J.; Sivadinarayana, C.; Wilson, O. M.; Yan, Z.; Goodman, D. W.; Crooks, R. M. Titania-Supported PdAu Bimetallic Catalysts Prepared from Dendrimer-Encapsulated Nanoparticle Precursors. *J. Am. Chem. Soc.* **2005**, *127*, 1380–1381.
40. Weir, M. G.; Knecht, M. R.; Frenkel, A. I.; Crooks, R. M. Structural Analysis of PdAu Dendrimer-Encapsulated Bimetallic Nanoparticles. *Langmuir* **2010**, *26*, 1137–1146.
41. Yin, Z.; Chi, M.; Zhu, Q.; Ma, D.; Sun, J.; Bao, X. Supported Bimetallic PdAu Nanoparticles with Superior Electrocatalytic Activity Towards Methanol Oxidation. *J. Mater. Chem. A* **2013**, *1*, 9157–9163.
42. Dash, P.; Bond, T.; Fowler, C.; Hou, W.; Coombs, N.; Scott, R. W. J. Rational Design of Supported PdAu Nanoparticle Catalysts from Structured Nanoparticle Precursors. *J. Phys. Chem. C* **2009**, *113*, 12719–12730.
43. Creighton, J. A.; Eadon, D. G. Ultraviolet-Visible Absorption Spectra of the Colloidal Metallic Elements. *J. Chem. Soc., Faraday Trans.* **1991**, *87*, 3881–3891.
44. Yin, Z.; Ma, D.; Bao, X. Emulsion-Assisted Synthesis of Monodisperse Binary Metal Nanoparticles. *Chem. Commun.* **2010**, *46*, 1344–1346.
45. Wei, T.; Wang, J.; Goodman, D. W. Characterization and Chemical Properties of Pd–Au Alloy Surfaces. *J. Phys. Chem. C* **2007**, *111*, 8781–8788.
46. Frenkel, A. I.; Nemzer, S.; Pister, I.; Soussan, L.; Harris, T.; Sun, Y.; Rafailovich, M. H. Size-Controlled Synthesis and Characterization of Thiol-Stabilized Gold Nanoparticles. *J. Chem. Phys.* **2005**, *123*, 184701.
47. Lei, Y.; Jelic, J.; Nitsche, L.; Meyer, R.; Miller, J. Effect of Particle Size and Adsorbates on the L3, L2 and L1 X-ray Absorption Near Edge Structure of Supported Pt Nanoparticles. *Top. Catal.* **2011**, *54*, 334–348.
48. Sun, Y.; Frenkel, A. I.; Isseroff, R.; Shonbrun, C.; Forman, M.; Shin, K.; Koga, T.; White, H.; Zhang, L.; Zhu, Y.; Rafailovich, M. H.; Sokolov, J. C. Characterization of Palladium Nanoparticles by Using X-ray Reflectivity, EXAFS, and Electron Microscopy. *Langmuir* **2006**, *22*, 807–816.
49. Newville, M. IFEFFIT: Interactive XAFS Analysis and FEFF Fitting. *J. Synchrotron Radiat.* **2001**, *8*, 322–324.
50. Beale, A. M.; Weckhuysen, B. M. EXAFS as a Tool to Interrogate the Size and Shape of Mono and Bimetallic Catalyst Nanoparticles. *Phys. Chem. Chem. Phys.* **2010**, *12*, 5562–5574.
51. Li, Y.; Zakharov, D.; Zhao, S.; Tappero, R.; Jung, U.; Elsen, A.; Baumann, P.; Nuzzo, R. G.; Stach, E. A.; Frenkel, A. I. Complex Structural Dynamics of Nanocatalysts Revealed in Operando Conditions by Correlated Imaging and Spectroscopy Probes. *Nat. Commun.* **2015**, *6*, 7583.
52. Yevick, A.; Frenkel, A. I. Effects of Surface Disorder on EXAFS Modeling of Metallic Clusters. *Phys. Rev. B: Condens. Matter Mater. Phys.* **2010**, *81*, 115451–115457.
53. Frenkel, A. I. Solving the 3D Structure of Metal Nanoparticles. *Z. Kristallogr.* **2007**, *222*, 605–611.
54. Petkov, V. Nanostructure by High-Energy X-Ray Diffraction. *Mater. Today* **2008**, *11*, 28–38.
55. Bedford, N.; Dablemont, C.; Viau, G.; Chupas, P.; Petkov, V. 3-D Structure of Nanosized Catalysts by High-Energy X-ray Diffraction and Reverse Monte Carlo Simulations: Study of Ru. *J. Phys. Chem. C* **2007**, *111*, 18214–18219.
56. Petkov, V.; Bedford, N.; Knecht, M. R.; Weir, M. G.; Crooks, R. M.; Tang, W.; Henkelman, G.; Frenkel, A. Periodicity and Atomic Ordering in Nanosized Particles of Crystals. *J. Phys. Chem. C* **2008**, *112*, 8907–8911.
57. Prasai, B.; Ren, Y.; Shan, S.; Zhao, Y.; Cronk, H.; Luo, J.; Zhong, C.-J.; Petkov, V. Synthesis-Atomic Structure-Properties Relationships in Metallic Nanoparticles by Total Scattering Experiments and 3D Computer Simulations: Case of Pt-Ru Nanoalloy Catalysts. *Nanoscale* **2015**, *7*, 8122–8134.
58. Petkov, V.; Shastri, S.; Shan, S.; Joseph, P.; Luo, J.; Zhong, C.-J.; Nakamura, T.; Herbani, Y.; Sato, S. Resolving Atomic Ordering Differences in Group 11 Nanosized Metals and Binary Alloy Catalysts by Resonant High-Energy X-ray Diffraction and Computer Simulations. *J. Phys. Chem. C* **2013**, *117*, 22131–22141.
59. Wang, L.-L.; Johnson, D. D. Predicted Trends of Core–Shell Preferences for 132 Late Transition-Metal Binary-Alloy Nanoparticles. *J. Am. Chem. Soc.* **2009**, *131*, 14023–14029.
60. Liao, H.; Fisher, A.; Xu, Z. J. Surface Segregation in Bimetallic Nanoparticles: A Critical Issue in Electrocatalyst Engineering. *Small* **2015**, *11*, 3221–3246.
61. Toshima, N.; Harada, M.; Yamazaki, Y.; Asakura, K. Catalytic Activity and Structural Analysis of Polymer-Protected Gold-Palladium Bimetallic Clusters Prepared by the Simultaneous Reduction of Hydrogen Tetrachloroaurate and Palladium Dichloride. *J. Phys. Chem.* **1992**, *96*, 9927–9933.
62. Dash, P.; Dehm, N. A.; Scott, R. W. J. Bimetallic PdAu Nanoparticles as Hydrogenation Catalysts in Imidazolium Ionic Liquids. *J. Mol. Catal. A: Chem.* **2008**, *286*, 114–119.
63. Chan, W. C., White, P. D. *Fmoc Solid Phase Peptide Synthesis: A Practical Approach*; Oxford University Press: New York, 2000.
64. Bhattacharjee, S.; Bruening, M. L. Selective Hydrogenation of Monosubstituted Alkenes by Pd Nanoparticles Embedded in Polyelectrolyte Films. *Langmuir* **2008**, *24*, 2916–2920.
65. Petkov, V. Rad, a Program for Analysis of X-Ray-Diffraction Data from Amorphous Materials for Personal Computers. *J. Appl. Crystallogr.* **1989**, *22*, 387–389.
66. Gereben, O.; Petkov, V. Reverse Monte Carlo Study of Spherical Sample Under Non-Periodic Boundary Conditions: The Structure of Ru Nanoparticles Based on X-Ray Diffraction Data. *J. Phys.: Condens. Matter* **2013**, *25*, 454211.